Model for the electroproduction of kaons and Λ's from the deuteron

Oren V. Maxwell
Department of Physics, Florida International University, Miami, Florida 33199, USA
(Received 10 May 2013; revised manuscript received 7 January 2014; published 10 February 2014)

A formalism is presented for the investigation of the reaction $ed \to e'K^+\Lambda n$ in the relativistic impulse approximation. The formalism is based on a tree-level, effective Lagrangian model for the underlying virtual photoproduction reaction amplitude which incorporates a variety of baryon resonances with spins up to $\frac{5}{2}$ and the two kaon resonances, $K^\star(892)$ and $K1(1270)$. The parameters of the model were fit to a large pool of proton photoproduction data from the CLAS, GRAAL, SAPHIR, and LEPS Collaborations and to CLAS data for the virtual photoproduction structure functions σ_U, σ_T, σ_L, σ_{TT}, σ_{LT}, and $\sigma_{LT'}$. The final-state Λn interaction is incorporated in the model by means of a three-dimensional overlap integral based on a simple phenomenological Λn potential. Results are presented for both the differential cross section, $d\sigma/d\Omega_K$, and the double differential cross section, $d\sigma/d\Omega_K dE_K$, for the virtual photoproduction of positive kaons and Λ's from the deuteron.

DOI: 10.1103/PhysRevC.89.024001 PACS number(s): 24.10.Jv, 25.10.+s, 25.30.Rw, 13.60.−r

I. INTRODUCTION

The electromagnetic production of kaons from small nuclear targets provides information that complements both electromagnetic pion production studies and studies of hypernuclei and has been a subject of interest for several decades. The bulk of activity in this area, both theoretical and experimental, has focused on reactions with a proton target, but much additional information can be extracted from reactions with more complex targets like the deuteron or ^{3}He. In particular, the bound proton inside a deuteron is quite different from a free proton, so that different fits to reactions with a proton target that are of comparable quality might yield substantially different results for reactions with a deuteron target. Moreover, the weak binding of the deuteron permits its use as a quasi-free-neutron source, and the presence of both a hyperon and a nucleon in the final state allows one to use the deuteron reaction to study the hyperon-nucleon interaction.

While the electromagnetic production of strangeness from the deuteron has received much less attention than that devoted to reactions with proton targets, its history is nearly as venerable. The first theoretical studies with deuteron targets, which focused on the role of final-state interactions, date back to the 1960s [1]. Most of the subsequent theoretical work has also focused on the photoproduction reaction, either in connection with model dependence and final-state interactions [2–6], or in connection with a neutron target [7,8]. Some of the more recent work has incorporated rescattering contributions in the photoproduction amplitude [9,10] or employed a Regge-inspired framework to study photoproduction [11].

By contrast the electroproduction of strangeness from the deuteron has received much less attention. To my knowledge, the earliest theoretical work was carried out by Hsiao and Cotanch, who studied the sensitivity of the calculated three- and four-fold differential cross sections to various inputs such as the kaon vertex, the deuteron wave function, and the final-state interaction [12]. A more recent work considered information that could be gleaned from a separation of the cross section into contributions from longitudinally and transversely polarized photons [13].

Experimental work on electromagnetic strangeness production from the deuteron has been quite limited. There were some early experiments carried out in the 1970s [14], but since then, there have been only two experimental efforts involving deuteron targets reported in the literature, both quite recent. A group at the Laboratory of Nuclear Science at Tohoku has studied the photoproduction of neutral kaons from the deuteron [15], and a Hall C experiment at Thomas Jefferson National Accelerator Facility (TJNAF) has yielded results for the electroproduction of Λ's and Σ's from a variety of nuclear targets including the deuteron [16].

Motivated by this experimental effort, I have developed a formalism for the reaction $ed \to e'K^+\Lambda n$ and employed it to calculate the differential cross section, $d\sigma/d\Omega_K$, and the double differential cross section, $d\sigma/d\Omega_K dE_K$, for the corresponding virtual photoproduction reaction in the center-of-mass (c.m.) frame of the virtual photon and the deuteron. The differential cross section has been obtained as a function of $\cos\theta_K$ for electron kinematics corresponding to the Hall C experiment and for two different values of the squared virtual photon 4-momentum q^2. Here θ_K is the angle between the kaon and the virtual photon in the c.m. frame. The double differential cross section has been obtained both as a function of $\cos\theta_K$ for several values of the kaon energy E_K and as a function of E_K for several values of $\cos\theta_K$, again with electron kinematics corresponding to the Hall C experiment and two values of q^2.

The formalism is based on a relativistic impulse approximation in which the virtual photoproduction process is assumed to involve only the proton in the deuteron with the neutron acting as a spectator. To represent the amplitude for virtual photoproduction from the proton, I employ a model developed previously to describe the electromagnetic production of Λ's from the proton [17–19]. This model is a tree-level, effective Lagrangian model which incorporates most of the well-established baryon resonances with masses below 2.1 GeV and spins up to $\frac{5}{2}$, the two kaon resonances, $K^\star(892)$ and $K1(1270)$, and several higher lying nucleon resonances. For the electroproduction process, the off-shell structure of the hadronic electromagnetic vertices is handled by means of

phenomenological form factors with parameters determined in the fit. The fitted data included a large pool of proton photoproduction data from the CLAS, GRAAL, SAPHIR, and LEPS Collaborations and CLAS electroproduction data for the virtual photoproduction structure functions σ_U, σ_T, σ_L, σ_{TT}, σ_{LT}, and $\sigma_{LT'}$. A brief summary of the model is presented in Sec. II. For a more complete description, the reader should consult Refs. [17–19].

Section III describes the relativistic impulse approximation for the virtual photoproduction of positive kaons and Λ's from the deuteron. After using energy-momentum conservation to fix the neutron 3-momentum and the Λ energy, the double differential cross section, $d\sigma/d\Omega_K dE_K$, is obtained by integrating over the outgoing Λ direction. In the evaluation of the relevant matrix elements, the deuteron wave function is treated nonrelativistically. Previous studies have demonstrated that relativistic effects associated with the deuteron wave function are less important than uncertainties associated with the reaction amplitude and final-state interactions [3,12]. In this work, final-state interactions are incorporated via a nonrelativistic overlap integral using a simple phenomenological potential employed previously by Li and Wright [3] to represent the Λn interaction.

Results for the differential and double differential cross sections are presented in Sec. IV. The bulk of the results have been obtained without final-state interactions, but I also present a sampling of results for the double differential cross section $d\sigma/d\Omega_K dE_K$ with the final Λn interaction included. This interaction is expected to be significant whenever the relative momentum between the neutron and the Λ is small.

II. VIRTUAL PHOTOPRODUCTION MODEL

Within the single-photon exchange approximation, the matrix element for the electroproduction of a kaon and a Λ from a proton target can be expressed as the contraction of a lepton current with a hadron current multiplied by the propagator of the intermediate virtual photon. The hadron current has the general form

$$h^\mu = e\bar{u}_{M_\Lambda}(p_\Lambda)\hat{t}^\mu u_{M_p}(p_p). \tag{1}$$

In the square of the matrix element, the lepton spin sums can be performed analytically after imposing current conservation by making use of the Dirac trace theorems. If one further imposes the extreme relativistic approximation on the electron kinematics, one finds that the complete squared matrix element can be expressed in terms of a virtual photoproduction matrix element. In particular, one obtains

$$\frac{1}{4}\sum_{\text{spins}}|\langle F|\hat{T}|I\rangle|^2 = \frac{e^2}{4m_e^2q^2}\frac{1}{\epsilon-1}\sum_{M_\Lambda M_p}|\langle f|\hat{t}_\gamma|i\rangle|^2, \tag{2}$$

where

$$\epsilon = \left(1-2\frac{\mathbf{q}^2}{q^2}\tan^2\frac{\Psi}{2}\right)^{-1} \tag{3}$$

is the tranverse photon polarization. Here q and $\mathbf{q}$ are respectively the photon 4-momentum and 3-momentum, Ψ is the electron scattering angle in the laboratory frame, and the factor $\frac{1}{4}$ arises from the average over the spin projections of the initial electron and proton. For experiments with no measured spin projections, the square of the virtual photon matrix element can be decomposed into combinations of hadron matrix elements through the relation

$$\begin{aligned}\frac{1}{2}\sum_{M_\Lambda M_p}|\langle f|\hat{t}_\gamma|i\rangle|^2 = \frac{1}{4}\sum_{M_\Lambda M_p}&[(|h_x|^2+|h_y|^2)\\ &+\epsilon(|h_x|^2-|h_y|^2)\cos 2\phi - 2\epsilon\frac{q^2}{q_0^2}|h_z|^2\\ &-\frac{2}{q_0}\sqrt{-2q^2\epsilon(1+\epsilon)}\,\mathrm{Re}(h_x h_z^\star)\cos\phi,\end{aligned} \tag{4}$$

where ϕ is the angle between the lepton and hadron planes, and the hadron matrix elements have been defined with respect to a coordinate system with the z axis in the direction of the photon 3-momentum and the baryon 3-momenta all lying in the xz plane.

The model employed in this work for the hadronic current is discussed in detail in Refs. [17–19]. It consists of s-channel, u-channel, and t-channel contributions, as depicted in Fig. 1. In each channel, the Born contributions are supplemented by nucleon resonances (s channel), hyperon resonances (u channel), or kaon resonances (t channel). A list of all the resonances included in the model can be found in the references cited above.

The various hadron amplitudes have the general structures

$$\begin{aligned}\hat{t}_s^\mu &= \sum_{N^\star}[\mathcal{V}_K^\dagger(p_K)D(p_s)\mathcal{V}_\gamma(q)]^\mu,\\ \hat{t}_u^\mu &= \sum_{Y^\star}[\mathcal{V}_\gamma^\dagger(q)D(p_u)\mathcal{V}_K(p_K)]^\mu,\\ \hat{t}_t^\mu &= \sum_{K^\star}[\mathcal{V}_{\gamma K}^\dagger(q,p_t)D_t(p_t)\mathcal{V}_{p\Lambda}(p_t)]^\mu,\end{aligned} \tag{5}$$

where the $\mathcal{V}$'s designate the interaction vertices and the D's the intermediate hadron propagators. The quantities $p_s = p_\Lambda + p_K$, $p_u = p_\Lambda - q$, and $p_t = q - p_K$ are the 4-momenta transferred in the s, u, and t channels respectively.

The interaction vertices, as well as the propagators, depend upon the spin and parity of the particular intermediate hadron considered. Detailed expressions for the various interaction vertices required may be found in Refs. [17–19]. For the spin-$\frac{1}{2}$ propagator, I employ a relativistic Breit-Wigner form with an energy- and momentum-dependent width included in the s-channel resonance contributions. The propagators for the spin-$\frac{3}{2}$ and spin-$\frac{5}{2}$ resonances are obtained from the spin-$\frac{1}{2}$ propagator by attaching appropriate spin projection operators. See Ref. [19] for detailed expressions. In the t channel, I employ the standard spin-0 propagator for the kaon and multiply this by the spin-1 projection operator to obtain the spin-1 propagator for the two kaon resonances included in the model.

The nucleon resonances excited in the s channel generally lie in kinematic regions where various decay channels are open. Resonance decays are accounted for through the

inclusion of energy- and momentum-dependent widths in the resonance propagators. These widths are obtained from a dynamical model that makes use of an effective Lagrangian to generate the energy and momentum dependence in various decay channels and fixes the on-shell normalizations of the widths using empirical branching ratio data. Details can be found in Ref. [17].

In electroproduction, the exchanged photon is off shell, so that in an effective Lagrangian treatment, it is necessary to include form factors at the electromagnetic vertices. The form factors used in this work are the same as those employed in Refs. [17–19] and are discussed in detail in those references. I note here that in the Born contributions to the matrix element, the inclusion of form factors requires the addition of counterterms to preserve current conservation. The prescription by which these are included is discussed in detail in Ref. [18].

The model summarized above has two sets of parameters that are fit to data. The first set consists of the products of the coupling strengths at the two interaction vertices of each contribution. Only the resonance couplings were treated as fitted parameters. For the Born coupling products, fixed values were employed, as discussed in Ref. [18]. The second set of parameters consists of the mass and coupling parameters associated with the electromagnetic form factors.

The fit data included a large set of photoproduction data from CLAS, SAPHIR, LEPS, and GRAAL plus recent electroproduction data from CLAS. The data was fit in a two-step iterative procedure that is described in Refs. [18,19]. In each step of the procedure, the χ^2 per degree of freedom was minimized. The degree of convergence of the procedure was measured by comparing the χ^2 values obtained in successive iterations. In practice it was found that the procedure converged quite well after only two iterations.

Three different fits were obtained by this procedure. The first two fits incorporate electron beam asymmetry data and differ in the set of nucleon resonances that was incorporated in the fit. In particular, the first fit included two resonances $N(2080)$ and $N(2200)$ that no longer appear in the particle data tables. The second fit does not include these two resonances. Tables of parameter values for these two fits can be found in Ref. [19]. The third fit from Ref. [18] is an earlier fit that did not include electron beam asymmetry data.

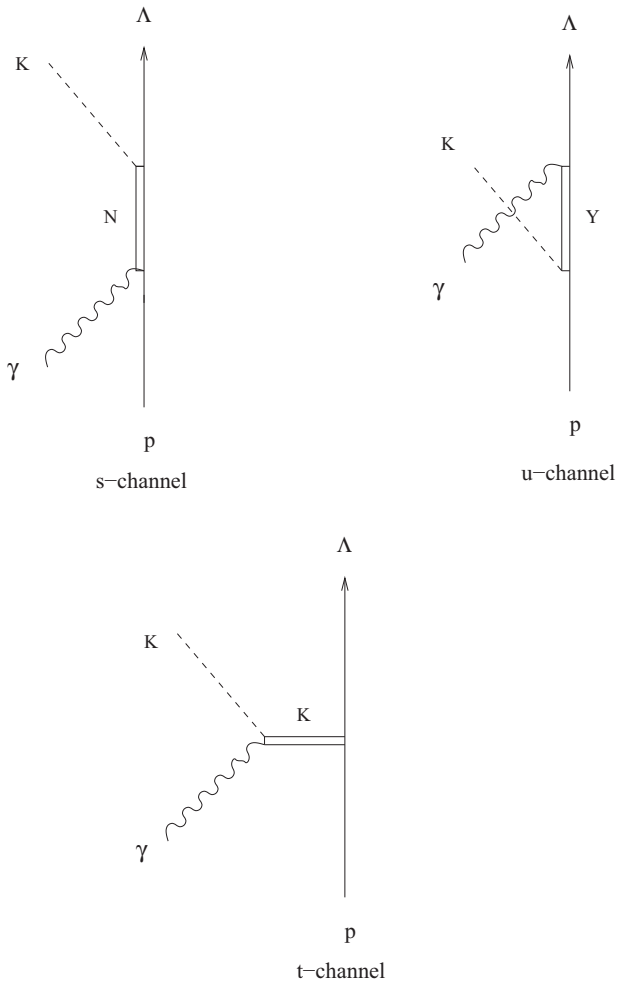

FIG. 1. Contributions to the amplitude for the reaction $\gamma p \to K^+\Lambda$.

III. VIRTUAL PHOTOPRODUCTION FROM THE DEUTERON

A. Matrix elements

To extract matrix elements for the electroproduction reaction $ed \to e'K^+\Lambda n$ from the virtual photoproduction model summarized in the previous section, I require a model for the deuteron wave function. In this work I employ a nonrelativistic wave function derived from the Paris NN interaction. Relativistic wave function effects in connection with electromagnetic strangeness production from the deuteron have been explored in several previous studies [2,3,12] and generally have been found to be less significant than other uncertainties associated with the models. I therefore feel justified in making use of a nonrelativistic bound-state wave function in what is otherwise a covariant formulation.

The deuteron wave function consists of an isospin factor multiplying a spin-spatial wave function,

$$\Psi_{M_d}(\mathbf{p_d}) = |(pn)I = 0\rangle \Phi_{M_d}(\mathbf{p_d}). \tag{6}$$

Here M_d and $\mathbf{p_d}$ are the deuteron spin projection and relative 3-momentum, respectively, and the isospin factor is given by

$$|(pn)I = 0\rangle = \frac{1}{\sqrt{2}}(|pn\rangle - |np\rangle). \tag{7}$$

The two terms in the last expression, in combination with the factor $\frac{1}{\sqrt{2}}$, yield an extra factor of 2 in the deuteron cross section as compared with the proton cross section.

The spin-spatial wave function can be further decomposed into products of spin and spatial wave functions,

$$\Phi_{M_d}(\mathbf{p_d}) = \sum_{M_S} \psi_{M_d M_S}(\mathbf{p_d})|1M_S\rangle, \tag{8}$$

with

$$\psi_{M_d M_S}(\mathbf{p_d}) = \sum_{L=0,2} \tilde{\phi}_L(p_d)(LM_L, 1M_S|1M_d)Y_{1M_L}(\hat{p}_d) \tag{9}$$

and

$$|1M_S\rangle = \sum_{M_p} \left(\frac{1}{2}M_p, \frac{1}{2}M_n|1M_S\right) \chi_{M_p}\chi_{M_n}, \tag{10}$$

where

$$\tilde{\phi}_L(p_d) = \sqrt{\frac{2}{\pi}} i^L \int_0^\infty r u_L(r) j_L(p_d r) dr \tag{11}$$

is the Fourier transform of the deuteron radial wave function.

I incorporate the deuteron wave function into the hadron current by defining the quantity

$$H^\mu = \sum_{M_S} \left(\frac{1}{2}M_p, \frac{1}{2}M_n|1M_S\right) \psi_{M_d M_S}(\mathbf{p_d}) h^\mu, \tag{12}$$

where h^μ is the hadron current defined by Eq. (1). Then, in analogy with Eq. (2), the spin-summed squared matrix element for the electroproduction reaction can be expressed in terms of matrix elements for the corresponding virtual photoproduction reaction through the relation

$$\frac{1}{6}\sum_{\text{spins}} |\langle F|\hat{T}|I\rangle|^2 = \frac{e^2}{6m_e^2 q^2}\frac{1}{\epsilon - 1} \sum_{M_d M_\Lambda M_n} |\langle f|\hat{t}_\gamma|i\rangle|^2, \tag{13}$$

where now the average over initial spin projections requires a factor $\frac{1}{6}$ rather than the factor $\frac{1}{4}$ appropriate for a proton target.

Because the hadron momenta in the reaction with a deuteron target are not confined to a single plane, the virtual photoproduction matrix element appearing in Eq. (13) contains more terms than that for a proton target; however, the procedure for obtaining the spin-summed squared matrix element is essentially the same. The result is

$$\frac{1}{3}\sum_{M_d M_\Lambda M_n} |\langle f|\hat{t}_\gamma|i\rangle|^2 = \frac{1}{6}\sum_{M_d M_\Lambda M_p} [(|H_x|^2 + |H_y|^2) + \epsilon(|H_x|^2 - |H_y|^2)\cos 2\phi - 2\epsilon\frac{q^2}{q_0^2}|H_z|^2$$
$$- 2\epsilon \text{Re}(H_x H_y^\star)\sin 2\phi - \frac{2}{q_0}\sqrt{-2q^2\epsilon(1+\epsilon)}[\text{Re}(H_x H_z^\star)\cos\phi - \text{Re}(H_y H_z^\star)\sin\phi], \tag{14}$$

where now ϕ is the angle between the lepton plane and the plane containing $\mathbf{p_K}$ and the total baryon 3-momentum $\mathbf{P_B} = \mathbf{p}_\Lambda + \mathbf{p_n}$.

In the model presented here, the deuteron wave function is defined in the deuteron rest frame, whereas the virtual photoproduction matrix elements are evaluated in the virtual photon-deuteron c.m. frame. Since the impulse approximation requires the neutron to be a spectator, its 4-momentum in the deuteron is just that of the outgoing neutron. This requirement, along with the requirement that the deuteron and virtual photon 3-momenta sum to zero in the c.m. frame, fixes the proton 4-momentum in the deuteron and thus, the relative deuteron momentum. The relative momentum in the deuteron rest frame can be obtained from the c.m. quantity by means of a Lorentz boost.

B. Cross section and kinematics

To facilitate comparison with the experimental result reported in Refs. [16], the virtual photoproduction cross section is evaluated in the c.m. of the virtual photon and the deuteron. In this frame, after using 3-momentum conservation to fix the neutron 3-momentum, I obtain

$$d\sigma_\gamma = K\frac{p_\Lambda}{E_n E_K}\frac{1}{3}\sum_{\text{spins}} |\langle f|\hat{t}_\gamma|i\rangle|^2 \delta(E_F - E_I) d^3p_\Lambda d^3p_K, \tag{15}$$

where p_Λ is the magnitude of the Λ 3-momentum, and

$$K = \frac{1}{4\pi^2}\frac{m_d m_\Lambda m_n}{R} \tag{16}$$

with

$$R = \sqrt{(s - q^2 - m_d^2)^2 - 4q^2 m_d^2}. \tag{17}$$

In the last expression, s is the squared c.m. energy (deuteron plus virtual photon), and q^2 is the square of the virtual photon 4-momentum.

In Eq. (15), I employ the energy conservation condition to fix the Λ energy. The Λ energy can be obtained from the Lorentz invariant quantity $S_{n\Lambda}$ defined as the scalar product of the Λ 4-momentum with the total 4-momentum of the outgoing baryons. In the virtual photon-deuteron c.m. frame, this quantity is given by the expression

$$S_{n\Lambda} = \tfrac{1}{2}(E_{n\Lambda}^2 - p_K^2 + m_\Lambda^2 - m_n^2), \tag{18}$$

where $E_{n\Lambda} = \sqrt{s} - E_K$. In terms of $S_{n\Lambda}$, energy conservation yields the result

$$E_\Lambda = \frac{1}{D^2}(E_{n\Lambda}S_{n\Lambda} \pm u\sqrt{S_{n\Lambda}^2 - m_\Lambda^2 D^2}), \tag{19}$$

where $D^2 = E_{n\Lambda}^2 - u^2$ with $u = |p_K \cos\theta_{\Lambda K}|$. Here $\theta_{\Lambda K}$ is the angle between the outgoing kaon and the Λ.

For kaon energies below a certain transition energy,

$$E_K^T = \frac{1}{2}\left[\sqrt{s} - m_\Lambda + \frac{m_K^2 - m_n^2}{\sqrt{s} - m_\Lambda}\right], \tag{20}$$

Eq. (19) has only one physical value. In particular, for $\theta_{\Lambda K} < \frac{\pi}{2}$, one has to choose the negative sign in Eq. (19), whereas for $\theta_{\Lambda K} > \frac{\pi}{2}$, one has to choose the positive sign. For kaon energies exceeding E_K^T, both signs yield physical values, but the range in $\theta_{\Lambda K}$ is restricted. In particular, $-1 \leqslant \cos\theta_{\Lambda K} \leqslant$

$-\frac{\alpha}{p_K}$, where

$$\alpha = \sqrt{E_{n\Lambda}^2 - \frac{S_{n\Lambda}^2}{m_\Lambda^2}}. \tag{21}$$

After imposing energy conservation to fix E_Λ, Eq. (15) reduces to

$$d\sigma_\gamma = K \sum_r \frac{p_K p_\Lambda^2}{m_\Lambda \sqrt{u^2-\alpha^2}} \frac{1}{3} \sum_{\text{spins}} |\langle f|\hat{t}_\gamma|i\rangle|^2 d\Omega_\Lambda dE_K d\Omega_K, \tag{22}$$

where the first sum is over the allowed values of E_Λ for particular E_K and $\theta_{\Lambda K}$.

In the experiment reported in Refs. [16], only the outgoing kaon is detected. Thus, to compare our model results with the data from that experiment, it is necessary to integrate over the outgoing Λ direction. The azimuthal part of the integral is unrestricted; in the $\cos\theta_{\Lambda K}$ integral, the range is determined by the value of E_K, as discussed above.

The $\cos\theta_{\Lambda K}$ integration is complicated numerically by the kinematic singularity that occurs when $u = \alpha$. To handle the singularity, I first observe that, using Eq. (19), the singular factor in Eq. (22) can be expanded as

$$\frac{p_\Lambda^2}{m_\Lambda\sqrt{u^2-\alpha^2}} = \frac{1}{\left(E_{n\Lambda}^2-u^2\right)^2}\left[E_{n\Lambda}^2 m_\Lambda \sqrt{u^2-\alpha^2} \pm 2S_{n\Lambda}E_{n\Lambda}u + \frac{S_{n\Lambda}^2 u^2}{m_\Lambda\sqrt{u^2-\alpha^2}}\right], \tag{23}$$

where the $\pm$ arises from the two solutions for E_Λ given by Eq. (19). Noting that only the last term in this expression is singular, I then divide the cross section into a part with a nonsingular integrand,

$$\frac{d\sigma_{NS}}{dE_K d\Omega_K} = p_K K \int d\Omega_\Lambda \sum_{r=\pm} \frac{1}{\left(E_{n\Lambda}^2-u^2\right)^2} \times \left[E_{n\Lambda}^2 m_\Lambda \sqrt{u^2-\alpha^2} + 2rS_{n\Lambda}E_{n\Lambda}u\right] \times \frac{1}{3}\sum_{\text{spins}} |\langle f|\hat{t}_\gamma|i\rangle|^2, \tag{24}$$

which can be integrated numerically without difficulty, and a part with a singular integrand,

$$\frac{d\sigma_S}{dE_K d\Omega_K} = p_K K \int d\Omega_\Lambda \sum_{r=\pm} \frac{S_{n\Lambda}^2 u^2}{\left(E_{n\Lambda}^2-u^2\right)^2} \frac{1}{m_\Lambda\sqrt{u^2-\alpha^2}} \times \frac{1}{3}\sum_{\text{spins}} |\langle f|\hat{t}_\gamma|i\rangle|^2. \tag{25}$$

Defining the quantity

$$\mathcal{M}(u) = \frac{S_{n\Lambda}^2 u^2}{m_\Lambda\left(E_{n\Lambda}^2-u^2\right)^2}\frac{1}{3}\sum_{\text{spins}} |\langle f|\hat{t}_\gamma|i\rangle|^2, \tag{26}$$

and noting that as $u \to \alpha$,

$$\frac{\mathcal{M}(u)-\mathcal{M}(\alpha)}{\sqrt{u^2-\alpha^2}} \to 0, \tag{27}$$

I can recast Eq. (25) as

$$\frac{d\sigma_S}{dE_K d\Omega_K} = p_K K \int d\Omega_\Lambda \frac{\mathcal{M}(u)-\mathcal{M}(\alpha)}{\sqrt{u^2-\alpha^2}} + p_K K \int_0^{2\pi} \mathcal{M}(\alpha) \int \frac{d\Omega_\Lambda}{\sqrt{u^2-\alpha^2}}. \tag{28}$$

The integrand in the first term of this expression is nonsingular, while the $\cos\theta_{\Lambda K}$ integral in the second term can be performed analytically. The resulting expression, when combined with the nonsingular part, yields the double differential cross section for the virtual photoproduction of a kaon and a Λ from the deuteron.

To get the corresponding differential cross section, the double differential cross section has to be integrated over the kaon energy. The integral is carried out from the kaon mass up to the maximum kaon energy given by

$$E_K^{\max} = \frac{1}{2\sqrt{s}}\left[s + m_K^2 - (m_\Lambda + m_n)^2\right]. \tag{29}$$

C. Incorporation of final-state interactions

To incorporate the final-state interaction between the outgoing neutron and Λ, I make use of a nonrelativistic overlap integral

$$\langle F|\hat{T}|I\rangle = \langle F|\hat{T}|I\rangle_{IA} + \sum_{M'_\Lambda M'_n} \int \frac{d^3k}{(2\pi)^{\frac{3}{2}}} \Psi_{M_\Lambda M_n M'_\Lambda M'_n}(\mathbf{p},\mathbf{k}) \langle F|\hat{T}|I\rangle_{IA}, \tag{30}$$

where the matrix element on the left is a function of the relative Λn 3-momentum $\mathbf{p}$, and the matrix element within the integral on the right is evaluated at the relative 3-momentum $\mathbf{k}$. The quantity Ψ, defined by the expression

$$\Psi_{M_\Lambda M_n M'_\Lambda M'_n}(\mathbf{p},\mathbf{k}) = \sum_{S=0,1} \left(\frac{1}{2}M_\Lambda \frac{1}{2}M_n|SM_S\right)\left(\frac{1}{2}M'_\Lambda \frac{1}{2}M'_n|SM_S\right)\psi_S(\mathbf{p},\mathbf{k}), \tag{31}$$

with

$$\psi_S(\mathbf{p},\mathbf{k}) = \int \frac{d^3r}{(2\pi)^{\frac{3}{2}}} \exp(i\mathbf{k}\cdot\mathbf{r})\phi_S^*(\mathbf{p},\mathbf{r}) - (2\pi)^{\frac{3}{2}}\delta(\mathbf{p}-\mathbf{k}), \tag{32}$$

is just the spin-summed Fourier transform of the final-state wave function with the plane wave part subtracted.

Introducing partial wave expansions into the integrand of Eq. (32) permits the angle integrals to be performed analytically, yielding

$$\psi_S(\mathbf{p},\mathbf{k}) = \sqrt{\frac{2}{\pi}}\sum_\ell (2\ell+1) R_{\ell S}(p,k) P_\ell(\cos\theta_{pk}), \tag{33}$$

with

$$R_{\ell S}(p,k) = \int_0^\infty r^2 dr \frac{u_{\ell S}^*(p,r)}{r} j_\ell(kr), \tag{34}$$

where $u_{\ell S}(p,r)$ is the radial part of the final state wave function. Asymptotically, the radial function $R_{\ell S}(p,k)$ has the form

$$R^{\rm asy}_{\ell S}(p,k) = \frac{\exp(-i\delta_{\ell S})\sin\delta_{\ell S}}{k^2 - p^2 + i\epsilon}\left(\frac{\delta_{\ell,\rm even}}{p} + \frac{\delta_{\ell,\rm odd}}{k}\right), \quad (35)$$

where $\delta_{\ell S}$ is the Λn phase shift. To facilitate the numerical evaluation of the radial integrals over r and k, the asymptotic part is subtracted from the integrand in Eq. (34) and the resulting integral multiplied by $k^2 - p^2$. This yields

$$\frac{k^2 - p^2}{(2\pi)^{\frac{3}{2}}}\psi_S(\mathbf{p},\mathbf{k}) = \frac{1}{2\pi^2}\sum_\ell (2\ell+1)\mathcal{R}_{\ell S}(p,k)P_\ell(\cos\theta_{pk}), \quad (36)$$

with

$$\mathcal{R}_{\ell S}(p,k) = (k^2 - p^2)R^{\rm rem}_{\ell S}(p,k) + \exp(-i\delta_{\ell S})\sin\delta_{\ell S}\left(\frac{\delta_{\ell,\rm even}}{p} + \frac{\delta_{\ell,\rm odd}}{k}\right), \quad (37)$$

where $R^{\rm rem}_{\ell S}$ is the difference between $R_{\ell S}$ and $R^{\rm asy}_{\ell S}$.

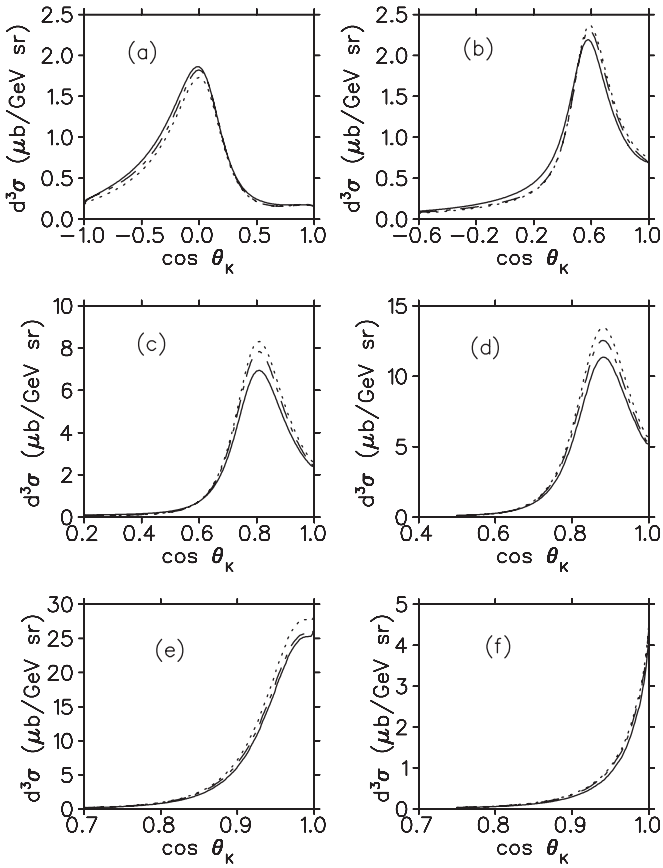

FIG. 2. $d\sigma/d\Omega_K dE_K$ vs $\cos\theta_K$ for $E_{\rm Lab} = 3.245$ GeV, $\sqrt{s} = 3.070$ GeV, $-q^2 = 0.350$ GeV^2, $\phi = 30^\circ$, and (a) $E_K = 0.675$ GeV, (b) $E_K = 0.750$ GeV, (c) $E_K = 0.800$ GeV, (d) $E_K = 0.820$ GeV, (e) $E_K = 0.850$ GeV, and (f) $E_K = 0.880$ GeV. In each panel, the solid, dash-dotted, and dotted curves were obtained with the three fits described in the text.

I now define a function $F_k^{M_\Lambda M_n}(\mathbf{p})$ through the relation

$$F_k^{M_\Lambda M_n}(\mathbf{p}) = \frac{k^2}{k+p}\int d\Omega_k \alpha_{M_\Lambda M_n}(\mathbf{p},\mathbf{k}), \quad (38)$$

with

$$\alpha_{M_\Lambda M_n}(\mathbf{p},\mathbf{k}) = \frac{k^2 - p^2}{(2\pi)^{\frac{3}{2}}}\sum_{M'_\Lambda M'_n}\Psi_{M_\Lambda M_n M'_\Lambda M'_n}(\mathbf{p},\mathbf{k})\langle F|\hat{T}|I\rangle_{IA}, \quad (39)$$

where, as in Eq. (30), the matrix element on the right of Eq. (39) is evaluated at the relative 3-momentum $\mathbf{k}$. In terms of this function, I finally obtain

$$\langle F|\hat{T}|I\rangle = \langle F|\hat{T}|I\rangle_{IA}\int_0^{k_{\rm max}}\frac{F_k^{M_\Lambda M_n}(\mathbf{p}) - F_p^{M_\Lambda M_n}(\mathbf{p})}{k-p}dk + F_k^{M_\Lambda M_n}(\mathbf{p})\left[i\pi + \ln\frac{k_{\rm max} - p}{p}\right]. \quad (40)$$

The use of a nonrelativistic final state prescription within a Lorentz covariant formalism requires some prescription for the baryon energies in the overlap integral. One prescription would be to require the neutron, which is just a spectator in the absence of final-state correlations, to remain on shell in the overlap integral. However, this choice forces the Λ to be far off shell in the overlap integral, even acquiring a negative

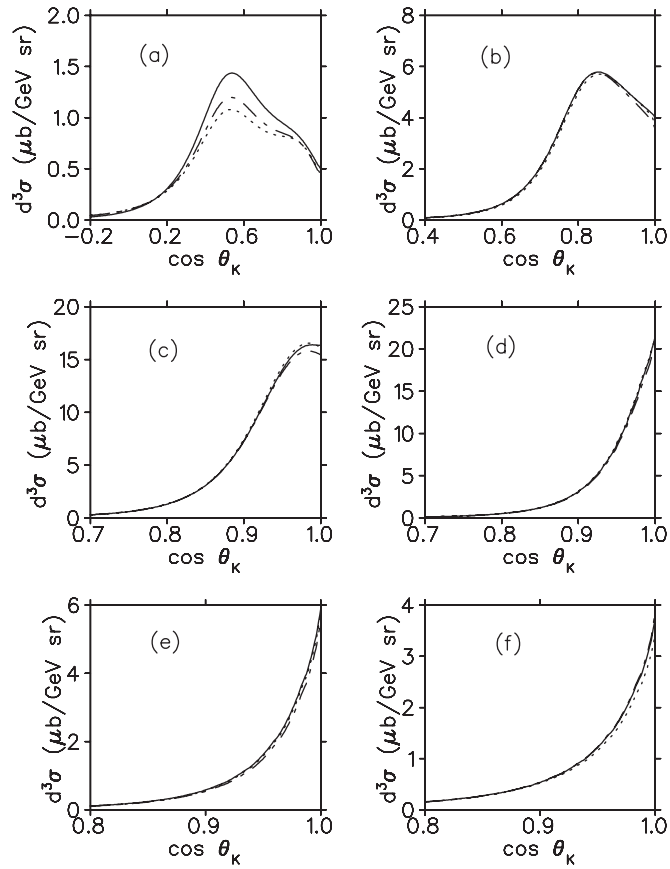

FIG. 3. $d\sigma/d\Omega_K dE_K$ vs $\cos\theta_K$ for the same kinematics as in Fig. 2 except that $-q^2 = 1.000$ GeV^2.

energy for large enough values of the relative momentum **k**. Moreover, the requirement that the neutron stay on shell in the overlap integral causes the overlap integral to converge very slowly as a function of $k_{\max}$. An alternative and, in my view, better prescription is to simply fix both E_Λ and E_n at their plane wave values. Then both the neutron and the Λ are off shell in the overlap integral, and it is found for the kinematics considered here that Eq. (40) yields a well-converged result with $k_{\max}$ of the order of 6 fm^{-1}.

To represent the Λn interaction, I employ a central potential consisting of a sum of attractive and repulsive Gaussians,

$$V_S(r) = -U_S \exp\left(-\frac{r^2}{\alpha_S^2}\right) + W_S \exp\left(-\frac{r^2}{\beta_S^2}\right), \qquad (41)$$

with parameter values $U_0 = 167.34$ MeV and $W_0 = 246.80$ MeV for $S = 0$, $U_1 = 132.42$ MeV, and $W_1 = 181.68$ MeV for $S = 1$, and $\alpha_S = 1.10$ and $\beta_S = 0.82$ for both spin states. This potential was used previously by Li and Wright [3] and was also employed in Ref. [6]. Li and Wright also investigated more elaborate potentials but obtained results similar to those obtained with Eq. (41).

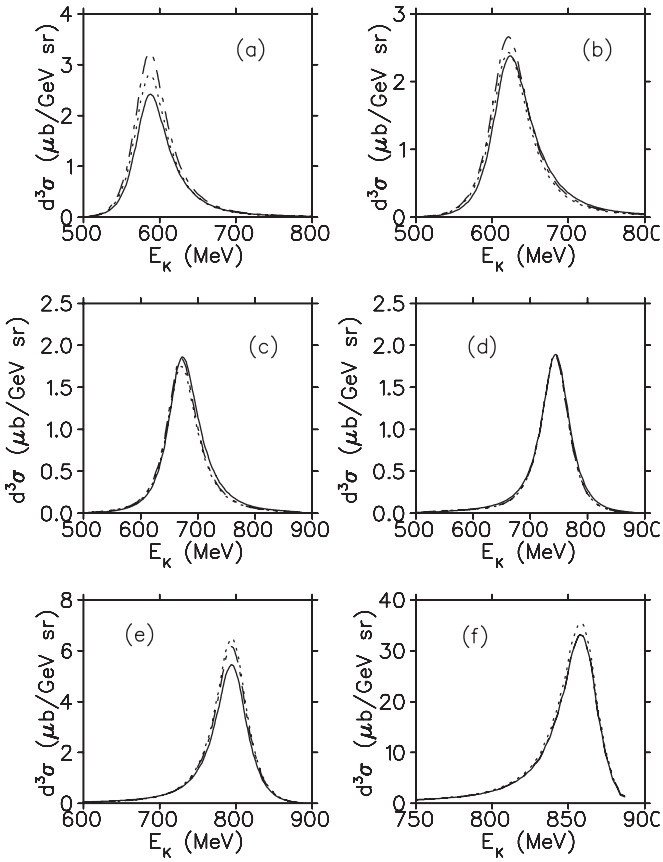

FIG. 4. $d\sigma/d\Omega_K dE_K$ vs E_K for $E_{\rm Lab} = 3.245$ GeV, $\sqrt{s} = 3.070$ GeV, $-q^2 = 0.350$ GeV^2, $\phi = 30^\circ$, and (a) $\cos\theta_K = -1.00$, (b) $\cos\theta_K = -0.50$, (c) $\cos\theta_K = 0.00$, (d) $\cos\theta_K = 0.50$, (e) $\cos\theta_K = 0.75$, and (f) $\cos\theta_K = 1.00$. In each panel, the solid, dash-dotted, and dotted curves were obtained with the three fits described in the text.

IV. RESULTS

In this section I report results for the differential and double differential cross sections discussed in the previous section. All of my results have been obtained for an incident electron beam energy, $E_{\rm Lab} = 3.245$ GeV, and a virtual photon-deuteron c.m. energy, $\sqrt{s} = 3.070$ GeV, corresponding to the central values used in the recent Hall C electroproduction experiment [16]. I have employed two different values for $-q^2$, the negative of the squared virtual photon 4-momentum, the lower of which, $-q^2 = 0.350$ GeV^2, is that used in the Hall C experiment. Most of my results have been obtained for $\phi = 30^\circ$, where ϕ is the angle between the lepton and baryon planes defined in Sec. II. However, since the Hall C data were obtained for a wide range in ϕ, rather than for specific values, I have also included results that are averaged over ϕ. As can be seen in Eq. (14), where the ϕ dependence in the squared matrix element is explicitly exhibited, averaging over ϕ eliminates all but three terms contributing to the squared matrix element, including all the interference terms between different components of the hadron current.

In the first four figures, I compare results generated with the three different fits discussed in the text. In each figure, the solid curves were obtained with the fit of Ref. [18], which did not include $\sigma_{LT'}$ data in the fit, the dash-dotted curve was obtained with the fit of Ref. [19], which included $\sigma_{LT'}$ data, and the dotted curve was obtained with the second fit of

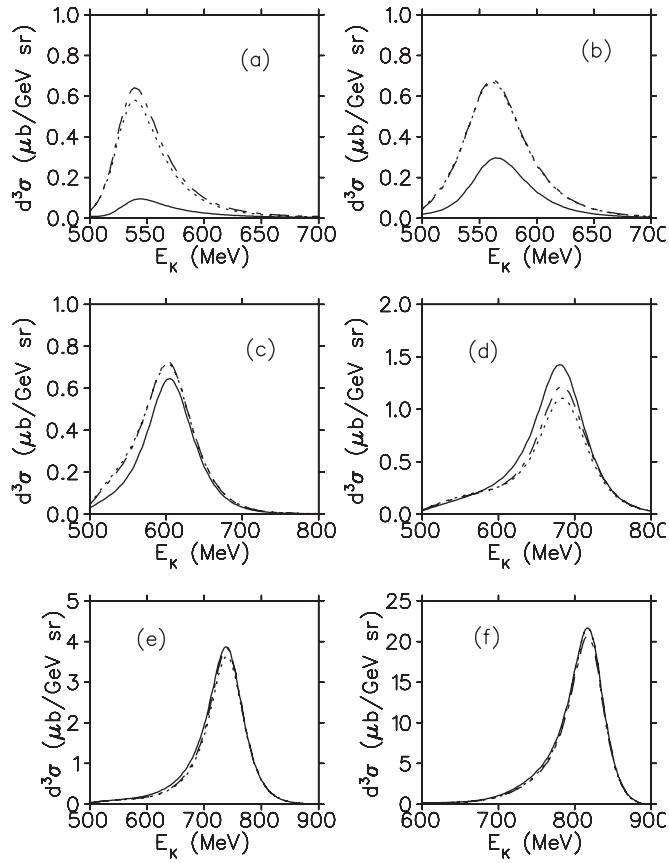

FIG. 5. $d\sigma/d\Omega_K dE_K$ vs E_K for the same kinematics as in Fig. 4 except that $-q^2 = 1.000$ GeV^2.

Ref. [19], which included $\sigma_{LT'}$ data but excluded the $N(2080)$ and $N(2200)$ resonances. None of the results exhibited in these four figures incorporate the Λn final-state interaction.

The first of these figures, Fig. 2, displays the double differential cross section as a function of $\cos\theta_K$ for several values of the kaon energy and for $-q^2 = 0.350$ GeV^2. As can be seen in the different panels, the double differential cross section is strongly peaked as a function of $\cos\theta_K$ with the location of the peak moving to more forward angles as the kaon energy increases. This behavior reflects the momentum distribution of the deuteron wave function and the fact that in the impulse approximation in the absence of final-state correlations, the proton momentum is fixed. As the similarities among the different curves in each figure indicate, the different fits investigated here yield similar results.

Figure 3 exhibits the double differential cross section as a function of $\cos\theta_K$ for the same kaon energies as in Fig. 2 but for a higher $-q^2$ value. As for the lower $-q^2$ value, the cross sections are peaked as functions of $\cos\theta_K$, but the peaks are broader and for the same kaon energy lie at more forward angles. As for the lower $-q^2$ value, there is a lack of sensitivity to the particular fit employed in the calculation.

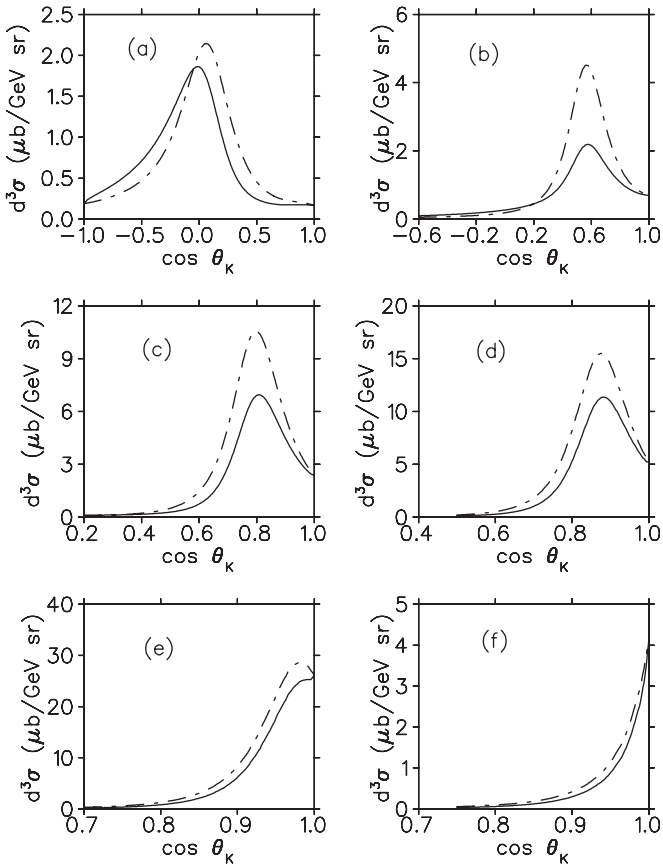

FIG. 6. $d\sigma/d\Omega_K dE_K$ vs $\cos\theta_K$ for $E_{\rm Lab} = 3.245$ GeV, $\sqrt{s} = 3.070$ GeV, $-q^2 = 0.350$ GeV^2, and (a) $E_K = 0.675$ GeV, (b) $E_K = 0.750$ GeV, (c) $E_K = 0.800$ GeV, (d) $E_K = 0.820$ GeV, (e) $E_K = 0.850$ GeV, and (f) $E_K = 0.880$ GeV. In each panel, the solid curve was obtained with $\phi = 30^\circ$, while the dash-dotted curve was obtained by averaging over ϕ.

The double differential cross section as a function of energy is shown in Fig. 4 for $-q^2 = 0.350$ GeV^2 and several kaon angles. Again the momentum distribution of the deuteron wave function, combined with the fixed proton momentum, leads to a sharp peak in the cross section. The fact that the peak moves to higher energies as the kaon angle moves to more forward angles is consistent with the results displayed earlier in Fig. 2. Comparing the curves in the various panels in Fig. 4 makes evident that at lower energy values and more backward angles, there is some sensitivity to the fit used in the calculations.

The energy dependence of the double differential cross section at $-q^2 = 1.0$ GeV^2 is exhibited in Fig. 5. As seen earlier in Fig. 3, the peaks in the cross section at the higher $-q^2$ value are broader than at the lower value. The upper two panels in Fig. 5 also reveal that at lower values of E_K, there is a more pronounced dependence on the fit employed for this $-q^2$ value.

The next four figures display the dependence of the double differential cross section on the treatment of ϕ, the angle between the lepton and hadron planes. In each of these figures, the solid curve was obtained with the fixed value $\phi = 30^\circ$, while the dot-dashed curve was obtained by averaging over ϕ. As for the first four figures, the results shown in these four figures do not incorporate the Λn final-state interaction.

In Fig. 6, the double differential cross section is shown as a function of $\cos\theta_K$ for several kaon energies and $-q^2 =$

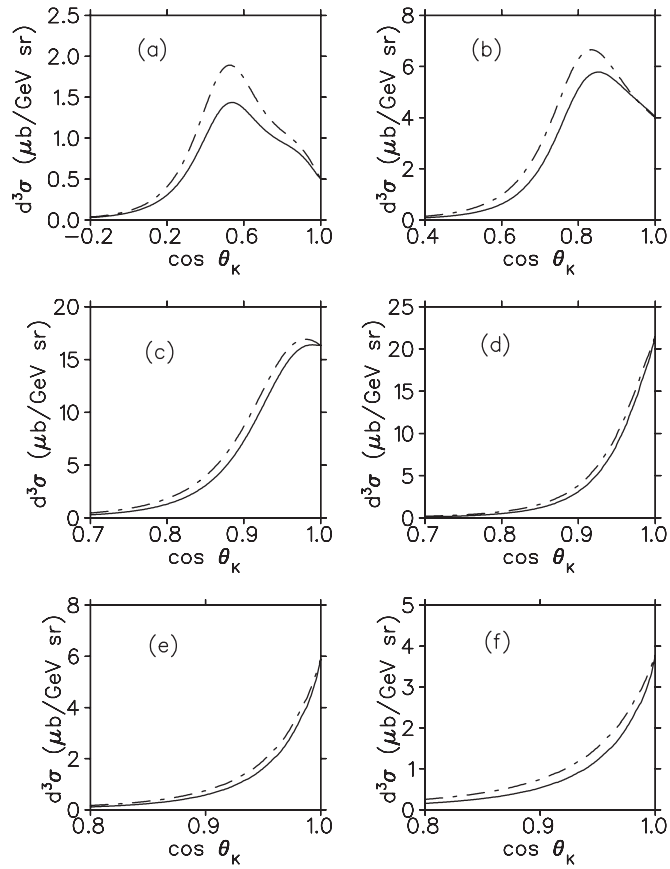

FIG. 7. $d\sigma/d\Omega_K dE_K$ vs $\cos\theta_K$ for the same kinematics as in Fig. 6 except that $-q^2 = 1.000$ GeV^2.

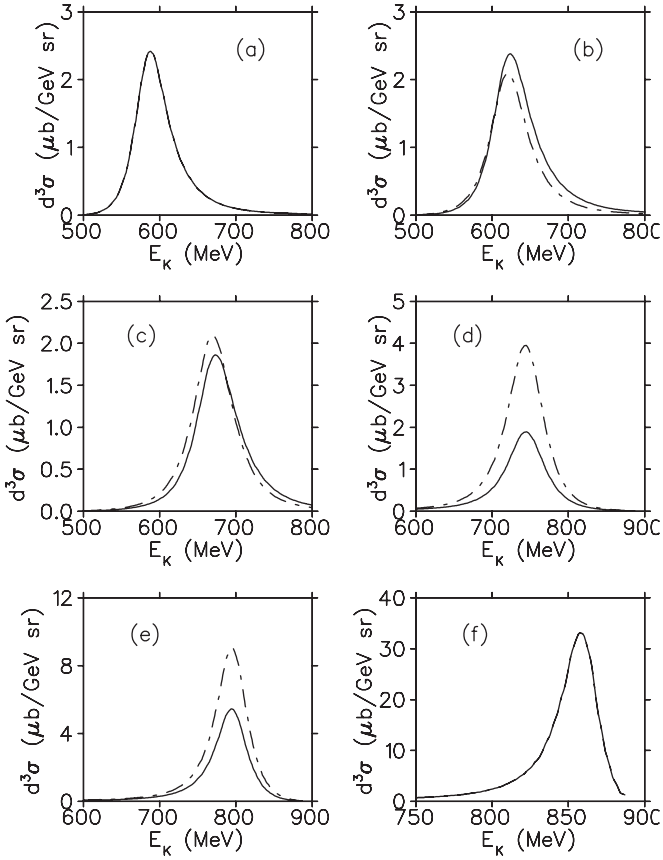

FIG. 8. $d\sigma/d\Omega_K dE_K$ vs E_K for $E_{\rm Lab} = 3.245$ GeV, $\sqrt{s} = 3.070$ GeV, $-q^2 = 0.350$ GeV^2, and (a) $\cos\theta_K = -1.00$, (b) $\cos\theta_K = -0.50$, (c) $\cos\theta_K = 0.00$, (d) $\cos\theta_K = 0.50$, (e) $\cos\theta_K = 0.75$, and (f) $\cos\theta_K = 1.00$. In each panel, the solid curve was obtained with $\phi = 30^\circ$ while the dash-dotted curve was obtained by averaging over ϕ.

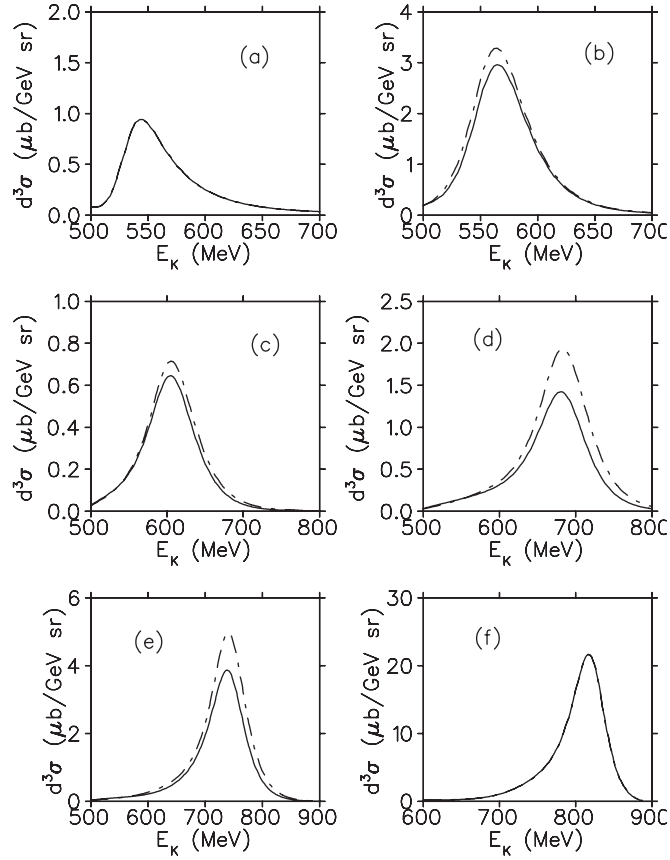

FIG. 9. $d\sigma/d\Omega_K dE_K$ vs E_K for the same kinematics as in Fig. 8 except that $-q^2 = 1.000$ GeV^2.

0.350 GeV^2. At the two larger energies, there is little difference in the two sets of results. At lower energies, the shapes of the peaks obtained are similar, but there are significant differences in the sizes of the peaks. Figure 7 reveals that these differences are less pronounced at $-q^2 = 1.00$ GeV^2.

The energy dependence of the double differential cross section for $-q^2 = 0.350$ GeV^2 and the two treatments of ϕ is exhibited in Fig. 8. Again, one can see that the shapes of the peaks are not affected by the treatment of ϕ, but that at certain angles, the sizes of the peaks are significantly influenced. Figure 9 displays the energy dependence of the cross section for $-q^2 = 1.00$ GeV^2. As seen earlier in Fig. 7, the dependence of the results on the treatment of ϕ is less pronounced at the larger $-q^2$ value.

The effect of the Λn final-state interaction is shown in the next two figures for both values of $-q^2$. All of the curves displayed in these two figures were obtained with the first fit of Ref. [19]. In each figure the curves in the left panels correspond to the choice $-q^2 = 0.350$ GeV^2 and the curves in the right panels correspond to $-q^2 = 1.00$ GeV^2.

Figure 10, which exhibits the angular distribution of the double differential cross section for different energies, reveals that the Λn final-state interaction can significantly affect the cross section but that this effect is strongly energy dependent. In general, the influence of the final-state interaction is greater at less forward angles; however, the position of the cross section peak as a function of $\cos\theta_K$ is not influenced much by the interaction.

In Fig. 11, which displays the double differential cross section as a function of E_K at several angles, it is clear that the final-state interaction has its greatest effect at the energies where the cross section peaks. At these energies, the final-state interaction increases the cross section substantially, in some cases by as much as a factor of 5.

The last two figures display the single differential cross section as a function of $\cos\theta_K$ for the same fit and the same two values of $-q^2$ as in the two previous figures. Because the incorporation of the final-state Λn interaction is extremely time-consuming, even for the double differential cross section, it has not been included in our results for the single differential cross section.

In Fig. 12 the dependence of the calculated cross section on the fit employed is shown. The strong forward peaking seen there arises from the strong forward peaking in the double differential cross section at the larger kaon energies and the fact that the cross section peaks are generally higher at the larger kaon energies. The near coincidence of the curves in

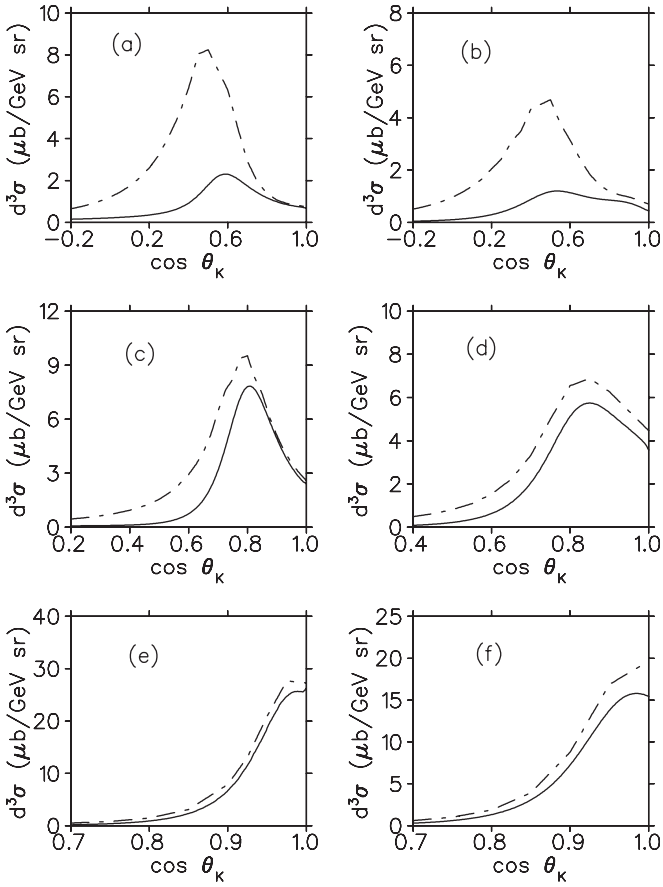

FIG. 10. $d\sigma/d\Omega_K dE_K$ vs $\cos\theta_K$ for $E_{\rm Lab} = 3.245$ GeV, $\sqrt{s} = 3.070$ GeV, $\phi = 30^\circ$, and (a) $E_K = 0.750$ GeV, $-q^2 = 0.350$ GeV^2, (b) $E_K = 0.675$ GeV, $-q^2 = 1.000$ GeV^2, (c) $E_K = 0.800$ GeV, $-q^2 = 0.350$ GeV^2, (d) $E_K = 0.750$ GeV, $-q^2 = 1.000$ GeV^2, (e) $E_K = 0.850$ GeV, $-q^2 = 0.350$ GeV^2, and (f) $E_K = 0.800$ GeV, $-q^2 = 1.000$ GeV^2. In each panel, the solid curve was obtained without the Λn interaction and the dash-dotted curve was obtained with the Λn interaction incorporated as described in the text.

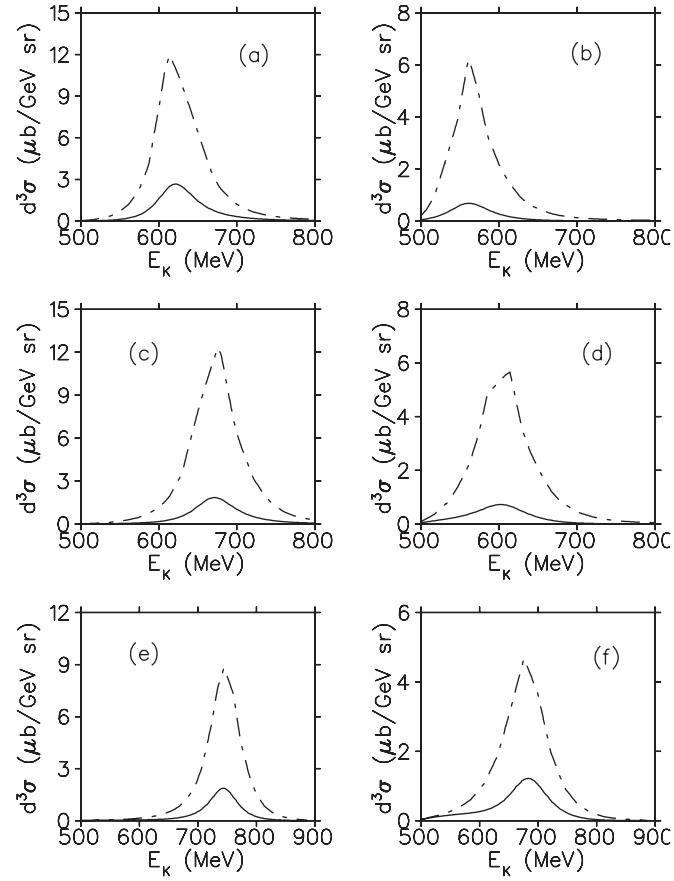

FIG. 11. $d\sigma/d\Omega_K dE_K$ vs E_K for $E_{\rm Lab} = 3.245$ GeV, $\sqrt{s} = 3.070$ GeV, $\phi = 30^\circ$, and (a) $\cos\theta_K = -0.50$, $-q^2 = 0.350$ GeV^2, (b) $\cos\theta_K = -0.50$, $-q^2 = 1.000$ GeV^2, (c) $\cos\theta_K = 0.00$, $-q^2 = 0.350$ GeV^2, (d) $\cos\theta_K = 0.00$, $-q^2 = 1.000$ GeV^2, (e) $\cos\theta_K = 0.50$, $-q^2 = 0.350$ GeV^2, and (f) $\cos\theta_K = 0.50$, $-q^2 = 1.000$ GeV^2. In each panel, the solid curve was obtained without the Λn interaction and the dash-dotted curve was obtained with the Λn interaction incorporated as described in the text.

each panel again indicates a lack of sensitivity to the particular fit employed.

The dependence of the cross section on the treatment of the angle ϕ is exhibited in Fig. 13. There is somewhat greater dependence on this aspect of the model than on the model fit employed, especially at the smaller $-q^2$ value, but the dependence is still quite modest.

The differential cross section for the virtual photoproduction of Λ's from the deuteron has only been measured at the single kaon laboratory angle, $\theta_{\rm Lab} = 1.7^\circ$. The differential cross section reported at this angle (in the virtual photon-deuteron c.m.) is 0.41 ± 0.02 $\mu b/sr$ [16].

As is well known, a single laboratory scattering angle can correspond to two different angles in the c.m., depending on the kinematics. To determine which kaon c.m. angles correspond to a specified kaon laboratory angle, it is necessary to boost the kaon momentum from the laboratory to the c.m. frame and then compare the resulting parallel and perpendicular components. When this is done, it is found that the differential cross section

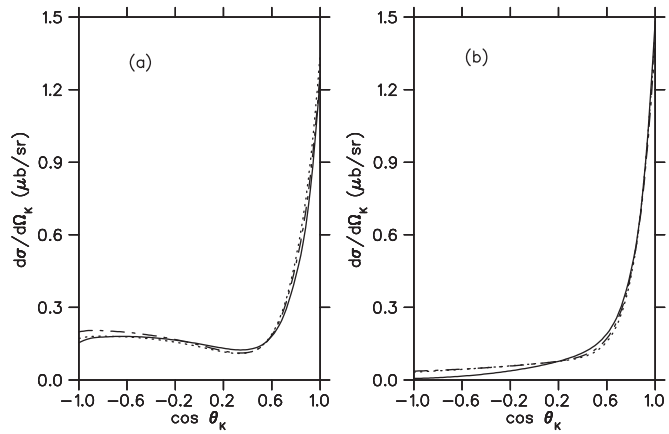

FIG. 12. $d\sigma/d\Omega_K$ vs $\cos\theta_K$ for $E_{\rm Lab} = 3.245$ GeV, $\sqrt{s} = 3.070$ GeV, $\phi = 30^\circ$, and (a) $-q^2 = 0.350$ GeV^2 and (b) $-q^2 = 1.000$ GeV^2. In each panel, the solid, dash-dotted, and dotted curves were obtained with the three fits described in the text.

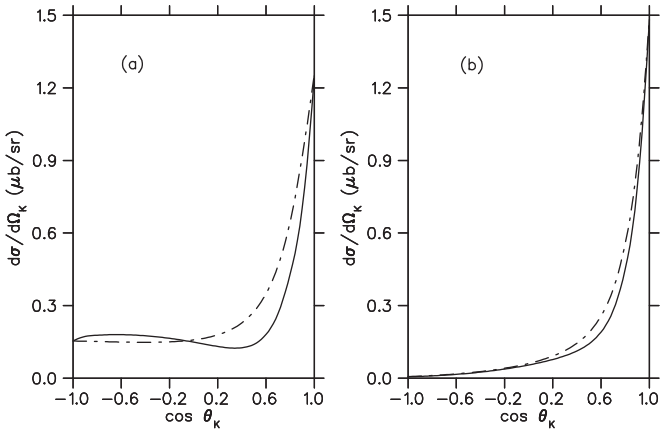

FIG. 13. $d\sigma/d\Omega_K$ vs $\cos\theta_K$ for $E_{\rm Lab} = 3.245$ GeV, $\sqrt{s} = 3.070$ GeV, and (a) $-q^2 = 0.350$ GeV^2 and (b) $-q^2 = 1.000$ GeV^2. In each panel, the solid curve was obtained with $\phi = 30^\circ$ while the dash-dotted curve was obtained by averaging over ϕ.

evaluated at $\theta_{\rm Lab} = 0^\circ$ receives contributions from both $\theta_{\rm c.m.} = 0^\circ$ and $\theta_{\rm c.m.} = 180^\circ$ only if $m_d\, p_K \leqslant m_K\, p_d$, where p_K and p_d are the 3-momenta evaluated in the c.m. frame. Since the ratio of m_K to m_d is quite small, this happens only at relatively small p_K, where the double differential cross section is small. Hence, the bulk of the contribution to the differential cross section at $\theta_{\rm Lab} = 0^\circ$ comes from $\theta_{\rm c.m.} = 0^\circ$. At $\theta_{\rm c.m.} = 0^\circ$, our ϕ averaged result for the differential cross section at $-q^2 = 0.350$ GeV^2 is 1.26 $\mu b/sr$, which is about a factor of three larger than the experimental result.

As indicated above, the differential cross results presented in Figs. 12 and 13 do not incorporate the Λn final-state interaction. While the influence of final-state interactions on the three-fold differential cross section in electroproduction (corresponding to the single differential cross section in virtual photoproduction) was found to be quite modest in an earlier work [12], the results exhibited in Figs. 10 and 11 suggest that the inclusion of the Λn final-state interaction in the single differential cross section would enhance the cross section rather than reduce it, thereby increasing the discrepancy with the empirical result.

In summary, I have developed a model for calculating the single and double differential cross sections for the virtual photoproduction of kaons and Λ's from the deuteron. The results obtained with this model are insensitive to the particular fit employed to represent the underlying virtual photoproduction reaction, at least within the range of fits considered here, and are sensitive to the treatment of ϕ, the angle between the hadron and lepton planes, only at smaller kaon energies. The inclusion of the Λn final-state interaction significantly enhances the calculated double differential cross section, particularly near the peaks in the energy distributions.

[1] F. M. Renard and Y. Renard, Nucl. Phys. B **1**, 389 (1967); Phys. Lett. B **24**, 159 (1967).
[2] R. A. Adelseck and L. E. Wright, Phys. Rev. C **39**, 580 (1989).
[3] X. Li and L. E. Wright, J. Phys. G **17**, 1127 (1991).
[4] H. Yamamura, K. Miyagawa, T. Mart, C. Bennhold, H. Haberzettl, and W. Glöckle, Phys. Rev. C **61**, 014001 (1999); K. Miyagawa, T. Mart, C. Bennhold, and W. Glockle, Mod. Phys. Lett. A **18**, 290 (2003).
[5] B. O. Kerbikov, Phys. At. Nucl. **64**, 1835 (2001).
[6] O. V. Maxwell, Phys. Rev. C **70**, 044612 (2004).
[7] X. Li, L. E. Wright, and C. Bennhold, Phys. Rev. C **45**, 2011 (1992).
[8] P. Bydzovsky, Int. J. Mod. Phys. E **19**, 2369 (2010).
[9] O. V. Maxwell, Phys. Rev. C **69**, 034605 (2004).
[10] A. Salam and H. Arenhovel, Phys. Rev. C **70**, 044008 (2004); A. Salam, K. Miyagawa, T. Mart, C. Bennhold, and W. Glockle, *ibid.* **74**, 044004 (2006); A. Salam, T. Mart, and K. Miyagawa, Mod. Phys. Lett. A **24**, 968 (2009).
[11] P. Vancraeyveld, L. De Cruz, J. Ryckebusch, and T. Van Cauteren, EPJ Web Conf. **3**, 03013 (2010).
[12] S. S. Hsiao and S. R. Cotanch, Phys. Lett. B **163**, 300 (1985); S. R. Cotanch and S. S. Hsiao, Nucl. Phys. A **450**, 419 (1986).
[13] T.-S. H. Lee, V. Stoks, B. Saghai, and C. Fayard, Nucl. Phys. A **639**, 247c (1998).
[14] A. M. Boyarski, R. Diebold, S. D. Ecklund, G. E. Fischer, Y. Murata, B. Richter, and M. Sands, Phys. Lett. B **34**, 547 (1971); C. J. Bebek *et al.*, Phys. Rev. D **15**, 594 (1977); D. J. Quinn, J. P. Rutherfoord, M. A. Shupe, D. J. Sherden, R. H. Siemann, and C. K. Sinclair, *ibid.* **20**, 1553 (1979).
[15] K. Tsukada *et al.*, Phys. Rev. C **78**, 014001 (2008).
[16] J. Reinhold *et al.*, Nucl. Phys. A **639**, 197c (1998); **684**, 470 (2001); B. Zeidman *et al.*, *ibid.* **691**, 37 (2001); F. Dohrmann *et al.*, Phys. Rev. C **76**, 054004 (2007).
[17] A. de la Puente, O. V. Maxwell, and B. A. Raue, Phys. Rev. C **80**, 065205 (2009).
[18] O. V. Maxwell, Phys. Rev. C **85**, 034611 (2012).
[19] O. V. Maxwell, Phys. Rev. C **86**, 064612 (2012).